Multi-grid phase field skin tumor segmentation in 3D ultrasound images

Khac Lan Nguyen, *MIA, University of La Rochelle,* Philippe Delachartre, *CREATIS, INSA Lyon,* and Michel Berthier, *MIA, University of La Rochelle*

Abstract—The aim of this paper is to present a new method for skin tumor segmentation in 3D ultrasound images. We consider a variational formulation the energy of which combines a diffuse interface phase field model (regularization term) and a log-likelihood computed using non parametric estimates (data attachment term). We propose a multi-grid implementation with exact solutions that has the advantage to avoid space discretization and numerical instabilities. The resulting algorithm is simple and is easy to implement in multi-dimensions. Concerning applications, we focus on skin tumor segmentation. The clinical dataset used for experiments is composed of 12 images with groundtruth given by a dermatologist. Comparisons with reference methods show that the proposed method is more robust to the choice of the volume initialization. Moreover, thanks to the flexibility introduced by the diffuse interface, the sensitivity increases by 12% if the initialization is inside the lesion, and the Dice index increases by 59%, if the initialization covers the entire lesion. These results show that this new method is well-designed to tackle the problem of underestimation of tumor volumes.

Index Terms—3D ultrasound images, tumor segmentation, phase field model, non-parametric estimation, multi-grid algorithm, exact solutions.

I. INTRODUCTION

ULtrasound imaging is widely used in medical diagnostic because it is non-invasive and low cost. However, it is well known that ultrasound images suffer from two major defects, the low contrast and the presence of speckle noise making processings more difficult. This explains why many works are still devoted to improve ultrasound image segmentation algorithms. In this paper, we focus on the problem of skin tumor segmentation in 3D ultrasound images [1], [2], [3], [4]. Ultrasounds have the advantage to probe at depths of 3mm or more while other non-invasive modalities, such as optical coherence tomography and reflectance confocal microscopy, are limited to a depth of 500 μm, which is insufficient to scan the bottom of deep lesions. Many works on this subject emphasize approaches based on level set methods [4]. These latters are well adapted to deal with the variability of lesion shapes and to remove structures due to speckle patterns. However, level set segmentations tend to underestimate the size of tumors and lack accuracy at the boundary of lesions. This is mainly due to the conservative property of the underlying dynamic.

Khac Lan Nguyen, MIA, University of La Rochelle, Av. A. Einstein, 17031 La Rochelle Cedex, France e-mail: khac.nguyen1@univ-lr.fr

Philippe Delachartre, CREATIS, INSA of LYON, 7 Av. J. Capelle, 69621 Lyon Cedex, France e-mail: philippe.delachartre@creatis.insa-lyon.fr

Michel Berthier, MIA, University of La Rochelle, Av. A. Einstein, 17031 La Rochelle Cedex, France e-mail: michel.berthier@univ-lr.fr

To overcome this drawback, we propose an alternative method based on the Cahn-Hilliard phase field model [5], [6]. This model is known to be relevant to describe phase transitions in various physical or chemical applications [7], [8]. We refer to [9], [10] and [11] for examples of applications to image processing. In [9] (resp. [10]) a double-well (resp. multiple-well) potential is added to the piecewise constant Mumford Shah functional. In both contributions [9] and [10] experiments are performed on simple 2D images. Note that the algorithm proposed in [10] appears to be difficult to implement. Dealing with 2D blood vessel images, the authors of [11] consider a phase field segmentation driven by a parametric statistical estimation. This latter is too predicted and is not relevant for the high frequency ultrasound images of skin tumors, as shown in [4].

In this work, the Allen-Cahn reaction-diffusion equation, *i.e.* the gradient descent of the Cahn-Hilliard energy, appears as a regularization term of a variational formulation. The data attachment term is given by a log-likelihood function measuring the dissimilarity of intensity distributions inside and outside the tumors. This approach is widely adopted in ultrasound image processing, see for instance [12], [13], [3], [14]. In the sequel, we use a nonparametric estimation based on Parzen estimates [15], [16]. This choice is motivated by arguments involving the specific characteristics of high frequency images of the skin. It is shown in [4] and [17] that the region surrounding a skin tumor is composed of several tissues of different natures that create heterogeneity in the medium. This phenomenon makes inadequate the use of classical parametric distributions such as Rayleigh, Rice, Nakagami or K distributions [18]. The main contributions of this work are:

1) A new variational model for skin tumor segmentation in 3D ultrasound images is proposed;

2) A new multi-grid implementation is presented which makes use of exact analytic solutions and avoid space discretization and numerical instabilities;

3) The resulting segmentation algorithm is simple to implement, with readily reproducible simulations, and is low cost in computational time.

Comparisons are made with state-of-the-art methods, namely, the Mumford-Shah Cahn-Hilliard (MSCH) segmentation [9] and the Adaptive Log-Likelihood Level-Set (AdLL) segmentation [4]. The 3D images used for the experiments were acquired at the Melanoma Skin Cancer Clinic, Hamilton Hill, Australia. These images are of size $300 \times 299 \times 832$ voxels, the last number corresponding to depth, with a lateral

(resp. depth) resolution of 50 μm (resp. 25 μm). They were chosen to be representative of the diversity of clinical cases and have been manually segmented by a dermatologist. For each one of the 3D images, 150 groundtruth contours are drawn in the $x - z$ planes (z is the vertical axis) and in the $y - z$ planes and two corresponding 3D volumes are obtained by interpolation. Using these two volumes one can evaluate the intra-observer variability of the segmentation. Results of the experiments show that the new LLCH, Log-Likelihood Cahn-Hilliard, algorithm has two major advantages over the reference ones:

1) The flexibility provided by the transition layer yields the best results in terms of sensitivity and Dice index. This means that the algorithm is well-designed to tackle the problem of underestimation of tumor volumes;

2) The multi-grid implementation with exact analytic solutions avoiding space discretization significantly improves the robustness to initialization, inside or covering the tumor.

The article is organized as follows. Section II is devoted to the presentation of the new LLCH-exact segmentation method from both the theoretical and numerical viewpoints. Then, we introduce in section III the measures used for the evaluation, describe first experiments and discuss the performance of the proposed multi-grid solver. Comparisons of our approach with the reference segmentation methods are presented in section IV. We end this paper by a discussion of the results and a conclusion.

II. THE PROPOSED SEGMENTATION METHOD: LLCH-EXACT SEGMENTATION

There exists a wide literature concerning phase transition and phase boundary evolution models. One of the most popular is the Level Set model [19]. As mentioned before, tumor segmentations based on level set approaches tend to underestimate the size of lesions. This is why we consider a new alternative model based on diffuse interface phase field. This latter aims at describing a process of phase separation, by which the two components of a binary fluid spontaneously separate and form domains pure in each component [7].

A. The variational formulation

We consider a classical variational formulation with energy given by
$$E(u) = E^{DA}(u) + \alpha E^{reg}(u) \qquad (1)$$
where $u = u(\mathbf{x}, t)$ denotes a space-time function and $\mathbf{x}$ (resp. t) is the 3D coordinate vector of the image (resp. the time variable). The term E^{DA} (resp. E^{reg}) is the data attachment term (resp. the regularization term). The parameter α ensures that the detected contour is smooth. In this work, E^{DA} is chosen so as to maximize the log-likelihood distance between intensity distributions inside and outside the tumor. The regularization term can be thought of as the area of the contour surface. Results on $\Gamma-$convergence (see for instance [20], [21]) allow to consider this regularization term as the limit, when ϵ tends to 0, of the Cahn-Hilliard energy
$$E_\epsilon^{CH}(u) = \int_\Omega \left(\epsilon \frac{|\nabla u|^2}{2} + \frac{1}{\epsilon} W(u) \right) d\mathbf{x} \qquad (2)$$

up to a multiplicative constant. The gradient flow of the Cahn-Hilliard energy (2), *i.e.* the Allen-Cahn reaction-diffusion equation [6], reads
$$\frac{\partial u}{\partial t} = \epsilon \Delta u - \frac{1}{\epsilon} W'(u) \qquad (3)$$
where W is the double-well potential, balanced and bistable, and W' is the derivative of W with respect to u. The symbol Δ is the Laplace operator, ϵ is the width of the transition layer. A classical choice for the potential is the polynomial $W(u) = u^2(1 - u)^2/2$, the two global minima of which, 0 and 1, correspond to the two phase equilibria. During the process, the phase field function u evolves in order to take the two distinct values, 0 and 1, in each of the phases. A diffuse interface of size ϵ is created in which the function u varies smoothly from 0 to 1. The target (resp. background) region is defined by: $\Omega_A = \{\mathbf{x} : u(\mathbf{x}, t) > 1/2, t \geq 0\}$ (resp. $\Omega_B = \{\mathbf{x} : u(\mathbf{x}, t) < 1/2, t \geq 0\}$). The moving interface (or transition layer) is defined by: $\Gamma_t = \{\mathbf{x} : u(\mathbf{x}, t) = 1/2, t \geq 0\}$. It is known that the Cahn-Hilliard energy Γ-converges, when ϵ tends to 0, to the product $c_W P$ where
$$P(u) = \int_\Gamma d\sigma, \quad c_W = \int_0^1 W(s) ds \qquad (4)$$
see for instance [20] or [21]. This means that minimizing the Cahn-Hilliard energy is equivalent to minimizing the area of the moving interface.

As said before, the data attachment term E^{DA} is chosen so as to maximize the log-likelihood of intensity distributions between the two regions Ω_A and Ω_B. Consequently, the two hypothesis of the likelihood are: H_0, all image intensities in Ω_A and Ω_B are i.i.d. random variables following a single distribution $P_{\Omega_A \cup \Omega_B}$, and H_1, the image intensities in the two regions Ω_A and Ω_B are i.i.d. random variables with different distributions P_A in Ω_A and P_B in Ω_B. The log-likelihood ratio can be written as
$$LL = \sum_{\mathbf{x} \in \Omega_A} \log P_A(I(\mathbf{x})) + \sum_{\mathbf{x}) \in \Omega_B} \log P_B(I(\mathbf{x})) + C \qquad (5)$$
where C is a constant that does not enter into consideration in the minimizing process. Using the equipartition theorem [22], we can replace $(1/|\Omega_A|) \sum_{\mathbf{x} \in \Omega_A} \log P_A(I(\mathbf{x}))$ by the entropy $\sum_I P_A(I) \log P_A(I)$, and the same for P_B. A simple computation shows that
$$\sum_I \hat{P}_A(I) \log \hat{P}_A(I) = \frac{1}{|\Omega_A|} \sum_{\mathbf{x} \in \Omega_A} \log \hat{P}_A(I(\mathbf{x}))$$
$$= Div_{KL}(\hat{P}_A || P_A) + \sum_I P_A(I) \log P_A(I) \qquad (6)$$
where Div_{KL} denotes the Kullback-Leibler divergence [22], and $\hat{P}_A$ is an estimate of P_A. Consequently, we may consider that the log-likelihood ratio is given by
$$LL = |\Omega_A| \sum_I \hat{P}_A(I) \log \hat{P}_A(I) + |\Omega_B| \sum_I \hat{P}_B(I) \log \hat{P}_B(I) \qquad (7)$$

The nonparametric estimation of the distributions $\hat{P}_A(I)$ and $\hat{P}_B(I)$ is performed using Parzen estimates [15], [16]

$$\hat{P}_A(I) = \frac{\int u^2 K_\lambda(I(\mathbf{x}) - I)d\mathbf{x}}{\int u^2 d\mathbf{x}} \qquad (8)$$

$$\hat{P}_B(I) = \frac{\int (u-1)^2 K_\lambda(I(\mathbf{x}) - I)d\mathbf{x}}{\int (u-1)^2 d\mathbf{x}} \qquad (9)$$

where K_λ is a centered Gaussian kernel with standard deviation λ. These Parzen estimates involve the phase field function u and from now on, we set $E^{DA}(u) = -LL(u)$.

B. The multi-grid implementation with exact solutions

Now, we explain how to implement the gradient descent of the variational formulation discussed above. The energy to be minimized reads

$$E_\epsilon(u) = -LL(u) + \frac{\alpha}{c_W} E^{CH}_\epsilon(u) \qquad (10)$$

Note that this functional is not convex and converges to $-LL(u) + \alpha P(u)$ when ϵ tends to zero (cf. equation (4)). The gradient descent is given by the Partial Differential Equation, PDE, $\partial u/\partial t = -\delta E_\epsilon/\delta u$, that is

$$\frac{\partial u}{\partial t} = 2u \log \hat{P}_A(I(\mathbf{x})) + 2(u-1) \log \hat{P}_B(I(\mathbf{x})) + \\ \frac{\alpha}{c_W} \left(\epsilon \Delta u - \frac{1}{\epsilon} W'(u) \right) \qquad (11)$$

(see appendix). Due to non convexity, the gradient flow converges to local minima depending on initializations.

It is important to notice at this stage that the theoretical model we propose allows us to optimize the implementation in the following sense. First, in order to reduce computational times, a crucial issue for practical use in a clinical context, we propose a multi-grid scheme. Second, thanks to a Lie splitting, we decompose the above PDE into three equations and compute the exact solutions of each one of these equations. Avoiding the use of space discretization, this approach ensures numerical stability for large time steps and improves robustness to initialization. The resulting new algorithm is simple and is easy to implement in multi-dimensions. The multi-grid scheme is given as follows. The image is decomposed into cells of size a whose coordinates are denoted $\bar{\mathbf{x}}$. We denote $\Omega_{\bar{\mathbf{x}}} = \{\mathbf{x} \in \bar{\mathbf{x}}\}$, $\hat{P}_{\bar{\mathbf{x}}}(I)$ the Parzen estimate of the intensity distribution in the volume $\Omega_{\bar{\mathbf{x}}}$ and $\bar{u} = \bar{u}(\bar{\mathbf{x}}, t)$. Writting $(\delta E_\epsilon/\delta \bar{u})(\bar{u}) = |\Omega_{\bar{\mathbf{x}}}|(\delta E_\epsilon/\delta u)(\bar{u})$, we obtain

$$\frac{\partial \bar{u}}{\partial t} = |\Omega_{\bar{\mathbf{x}}}| \left[\frac{\delta S_A}{\delta u}(\bar{u}) + \frac{\delta S_B}{\delta u}(\bar{u}) + \frac{\alpha}{c_W}\left(\epsilon \Delta \bar{u} - \frac{1}{\epsilon}W'(\bar{u})\right) \right] \qquad (12)$$

where

$$S_A = |\Omega_A| \sum_I \hat{P}_A(I) \log \hat{P}_A(I)$$
$$S_B = |\Omega_B| \sum_I \hat{P}_B(I) \log \hat{P}_B(I) \qquad (13)$$

The following equation must be satisfied

$$|\Omega_{\bar{\mathbf{x}}}| \frac{\delta S_A}{\delta u}(\bar{u}) = 2\bar{u}(\sum_{\mathbf{x} \in \bar{\mathbf{x}}} \log \hat{P}_A(I(\mathbf{x}))) \qquad (14)$$

and the same for S_B. Using the approximation

$$\sum_{\mathbf{x} \in \bar{\mathbf{x}}} \log \hat{P}_A(I(\mathbf{x})) = |\Omega_{\bar{\mathbf{x}}}| \sum_I P_{\bar{\mathbf{x}}}(I) \log \hat{P}_A(I) \qquad (15)$$

we deduce

$$\frac{\delta S_A}{\delta u}(\bar{u}) = 2\bar{u} \sum_I \hat{P}_{\bar{\mathbf{x}}}(I) \log \hat{P}_A(I) \qquad (16)$$

and

$$\frac{\delta S_B}{\delta u}(\bar{u}) = 2(\bar{u}-1) \sum_I \hat{P}_{\bar{\mathbf{x}}}(I) \log \hat{P}_B(I) \qquad (17)$$

Finally, the multi-grid flow reads

$$\frac{\partial \bar{u}}{\partial t} = 2\bar{u}|\Omega_{\bar{\mathbf{x}}}| \sum_I \hat{P}_{\bar{\mathbf{x}}}(I) \log \hat{P}_A(I) \\ + 2(\bar{u}-1)|\Omega_{\bar{\mathbf{x}}}| \sum_I \hat{P}_{\bar{\mathbf{x}}}(I) \log \hat{P}_B(I) \\ - |\Omega_{\bar{\mathbf{x}}}| \frac{\alpha}{\epsilon c_W} W'(\bar{u}) \\ + |\Omega_{\bar{\mathbf{x}}}| \frac{\epsilon \alpha}{c_W} \left(\frac{\partial^2 \bar{u}}{a^2 \partial \bar{x}^2} + \frac{\partial^2 \bar{u}}{a^2 \partial \bar{y}^2} + \frac{\partial^2 \bar{u}}{a^2 \partial \bar{z}^2} \right) \qquad (18)$$

where $\bar{\mathbf{x}} = (\bar{x}, \bar{y}, \bar{z})$ is a coordinate vector on a grid cell. Thanks to a Lie splitting, the equation (18) can be split into three equations [23]. The first and the second ones are first order Ordinary Differential Equations, ODE, and correspond to the data attachment and reaction terms (see lines 3 and 4 of Algorithm 1 below). Using Fourier transform, the third equation can also be seen as a first order ODE. It corresponds to the diffusion term (see line 5 of Algorithm 1 below). Now, we detail how to obtain exact solutions of these ODE.

1) Exact solutions of the data attachment term: Under the assumption that

$$T_A(\bar{\mathbf{x}}) = 2 \sum_I \hat{P}_{\bar{\mathbf{x}}}(I) \log(\hat{P}_A(I)\hat{P}_B(I)) \qquad (19)$$

and

$$T_B(\bar{\mathbf{x}}) = 2 \sum_I \hat{P}_{\bar{\mathbf{x}}}(I) \log(\hat{P}_B(I)) \qquad (20)$$

are constant in a discrete time interval $[t_n, t_{n+1}]$, the first ODE can be written as

$$\frac{\partial \bar{u}}{\partial t} = \bar{u}(\bar{\mathbf{x}}, t) H_A(\bar{\mathbf{x}}) - H_B(\bar{\mathbf{x}}) \qquad (21)$$

where $H_A = |\Omega_{\bar{\mathbf{x}}}|T_A$ and $H_B = |\Omega_{\bar{\mathbf{x}}}|T_B$. Solutions are given by

$$\bar{u}(\bar{\mathbf{x}}, t) = \left(\bar{u}_0(\bar{\mathbf{x}}) - \frac{H_B(\bar{\mathbf{x}})}{H_A(\bar{\mathbf{x}})} \right) e^{H_A(\bar{\mathbf{x}})t} + \frac{H_B(\bar{\mathbf{x}})}{H_A(\bar{\mathbf{x}})} \qquad (22)$$

with $\bar{u}_0(\bar{\mathbf{x}}) = \bar{u}(\bar{\mathbf{x}}, 0)$. Writing $t_{n+1} = t_n + \delta t$, this leads to the discrete iteration

$$U^{n+1}(\bar{\mathbf{x}}) = \left(U^n(\bar{\mathbf{x}}) - \frac{H_B(\bar{\mathbf{x}})}{H_A(\bar{\mathbf{x}})} \right) e^{H_A(\bar{\mathbf{x}})\delta t} + \frac{H_B(\bar{\mathbf{x}})}{H_A(\bar{\mathbf{x}})} \qquad (23)$$

where $U^n(\bar{\mathbf{x}}) \approx \bar{u}(\bar{\mathbf{x}}, t^n)$.

2) Exact solutions of the reaction term: Using $W'(\bar{u}) = \bar{u}(1-\bar{u})(1-2\bar{u})$, we have

$$\frac{\partial \bar{u}}{\partial t} = -|\Omega_{\bar{\mathbf{x}}}|\frac{\alpha}{\epsilon c_W}(\bar{u}(1-\bar{u})(1-2\bar{u})) \quad (24)$$

This equation has three stationary solutions given by $\bar{u}(\bar{\mathbf{x}}, t) = \bar{u}(\bar{\mathbf{x}}, 0) = \bar{u}_0(\bar{\mathbf{x}}) = 0, 1/2, 1$. The first and the last ones are of no interest because $0 \leq \bar{u}(\bar{\mathbf{x}}, t) \leq 1$, for all $\bar{\mathbf{x}}$ and t. Simple computations show that the solutions of (24) are given by

$$\begin{cases} \bar{u}(\bar{\mathbf{x}}, t) = 1/2 & \text{if } \bar{u}_0(\bar{\mathbf{x}}) = 1/2 \\[2mm] \bar{u}(\bar{\mathbf{x}}, t) = \dfrac{\sqrt{1+4c(t,\epsilon,\bar{u}_0)}+1}{2\sqrt{1+4c(t,\epsilon,\bar{u}_0)}} & \text{if } \bar{u}_0(\bar{\mathbf{x}}) > 1/2 \\[3mm] \bar{u}(\bar{\mathbf{x}}, t) = 1 - \dfrac{\sqrt{1+4c(t,\epsilon,\bar{u}_0)}+1}{2\sqrt{1+4c(t,\epsilon,\bar{u}_0)}} & \text{if } \bar{u}_0(\bar{\mathbf{x}}) < 1/2 \end{cases} \quad (25)$$

where:

$$c(t,\epsilon,\bar{u}_0(\bar{\mathbf{x}})) = \frac{\bar{u}_0(\bar{\mathbf{x}})(1-\bar{u}_0(\bar{\mathbf{x}}))}{(1-2\bar{u}_0(\bar{\mathbf{x}}))^2}e^{-\frac{\alpha|\Omega_{\bar{\mathbf{x}}}|t}{\epsilon c_W}} \quad (26)$$

As before, we denote $t_{n+1} = t_n + n\delta_t$ and $U^n(\bar{\mathbf{x}}) \approx \bar{u}(\bar{\mathbf{x}}, t^n)$. We set

$$g_C^+ = \frac{\sqrt{1+4C}+1}{2\sqrt{1+4C}}, \; g_C^- = 1 - \frac{\sqrt{1+4C}+1}{2\sqrt{1+4C}} \quad (27)$$

with

$$C = U^n(1-U^n)/(1-2U^n)^2 e^{-\frac{\alpha|\Omega_{\bar{\mathbf{x}}}|\delta t}{\epsilon c_W}} \quad (28)$$

The discrete iteration obtained from (25) is given by

$$U^{n+1} = \frac{1}{2}\mathcal{X}_{\{U^n=1/2\}} + g_C^+\mathcal{X}_{\{U^n>1/2\}} + g_C^-\mathcal{X}_{\{U^n<1/2\}} \quad (29)$$

where $\mathcal{X}_\mathcal{S}$ is the caracteristic function of the set $\mathcal{S}$, *i.e.* it is equal to 0 (resp. 1) outside $\mathcal{S}$ (resp. inside $\mathcal{S}$).

3) Exact solutions of the diffusion term: The equation

$$\frac{\partial \bar{u}}{\partial t} = |\Omega_{\bar{\mathbf{x}}}|\frac{\epsilon\alpha}{c_W}\left(\frac{\partial^2 \bar{u}}{a^2\partial\bar{x}^2} + \frac{\partial^2 \bar{u}}{a^2\partial\bar{y}^2} + \frac{\partial^2 \bar{u}}{a^2\partial\bar{z}^2}\right) \quad (30)$$

is solved with periodic boundary conditions. In the Fourier domain, this equation is the ODE

$$\frac{\partial \widehat{u}}{\partial t} = -4\pi^2|\Omega_{\bar{\mathbf{x}}}|\frac{\epsilon\alpha}{c_W}\left|\frac{\bar{\mathbf{k}}}{a}\right|^2\widehat{u} \quad (31)$$

with $\bar{\mathbf{k}} = (k_{\bar{x}}, k_{\bar{y}}, k_{\bar{z}})$ the Fourier variable, $\widehat{u} = \widehat{u}(\bar{\mathbf{k}}, t)$ and

$$|\bar{\mathbf{k}}/a|^2 = (k_{\bar{x}}/a)^2 + (k_{\bar{y}}/a)^2 + (k_{\bar{z}}/a)^2 \quad (32)$$

The solutions are given by

$$\widehat{u}(\bar{\mathbf{k}}, t) = \widehat{u}(\bar{\mathbf{k}}, 0)e^{-4\pi^2|\Omega_{\bar{\mathbf{x}}}|\frac{\epsilon\alpha}{c_W}\left|\frac{\bar{\mathbf{k}}}{a}\right|^2 t} \quad (33)$$

and lead to the discrete iteration

$$U^{n+1} = IFFT(G(\bar{\mathbf{k}})FFT(U^n)) \quad (34)$$

where, as above, $t_{n+1} = t_n + n\delta_t$, $U^n(\bar{\mathbf{x}}) \approx \bar{u}(\bar{\mathbf{x}}, t^n)$, and

$$G(\bar{\mathbf{k}}) = e^{-4\pi^2|\Omega_{\bar{\mathbf{x}}}|\frac{\epsilon\alpha}{c_W}\left|\frac{\bar{\mathbf{k}}}{a}\right|^2\delta t} \quad (35)$$

In (34), FFT (resp. IFFT) denotes the Fast Fourier Transform (resp. the Inverse Fast Fourier Transform). Finally, the new algorithm that we propose, using multi-grid implementation and exact solutions, is described as follows. The initialization $U^0 \approx \bar{u}(\bar{\mathbf{x}}, 0)$ is the caracteristic function of the initialization volume.

Algorithm 1: LLCH-exact segmentation

---

1) **Input:** $U^{n=0}$, δt, ϵ, α and I
2) **For:** $n = 1, ...,$ until convergence **do**
3)   Computation of the data attachment term, see (23):

$$U^n \leftarrow \left(U^n - \frac{T_B}{T_A}\right)\exp\left(2|\Omega_{\bar{\mathbf{x}}}|T_A\delta t\right) + \frac{T_B}{T_A}$$

4)   Computation of the reaction term, see (29):

$$U^n \leftarrow \frac{1}{2}\mathcal{X}_{\{U^n=1/2\}} + g_C^+\mathcal{X}_{\{U^n>1/2\}} + g_C^-\mathcal{X}_{\{U^n<1/2\}}$$

5)   Computation of the diffusion term, see (34):

$$U^{n+1} = IFFT(G(k)FFT(U^n))$$

6) **End for**
7) **Output:** U^{n+1}

III. EVALUATION OF THE PROPOSED LLCH-EXACT ALGORITHM

In this and the following sections, the performance criteria of the segmentation is evaluated with four measures.

- The Dice (or Sorensen-Dice) index is an indicator of the accuracy of a segmented volume Ω with respect to a reference volume R. It is given by $D(\Omega, R) = 2|\Omega \cap R|/(|\Omega| + |R|)$. The Dice index can be expressed as the harmonic mean of the sensitivity S and the precision P.

- The sensitivity S is defined by $S(\Omega, R) = |\Omega \cap R|/|R|$.

- The precision P reads $P(\Omega, R) = |\Omega \cap R|/|\Omega|$. We thus have:

$$D = 2/(1/S + 1/P) \quad (36)$$

- The Mean Absolute Distance allows to determine if the boundary of the segmented volume fits well with the boundary of the reference volume. Let $N_{\partial\Omega}$ (resp. $N_{\partial R}$) denotes the number of voxels in the boundary $\partial\Omega$ (resp. ∂R) of the segmented (resp. reference) volume. The (symetric) Mean Absolute Distance $\text{MAD}(\Omega, R)$ is defined by:

$$\text{MAD}(\Omega, R) = \sum_{x \in \partial\Omega}\frac{d(\mathbf{x}|R)}{2\text{surf}(\partial\Omega)} + \sum_{x \in \partial R}\frac{d(\mathbf{x}|\Omega)}{2\text{surf}(\partial R)} \quad (37)$$

In this definition, $d(\mathbf{x}|R) = \min_{\mathbf{x'} \in \partial R}\|\mathbf{x'} - \mathbf{x}\|$ is the distance of the point $\mathbf{x}$ to the boundary ∂R, and the same replacing R by Ω. The terms $\text{surf}(\partial R)$ and $\text{surf}(\partial\Omega)$ denote the number of voxels in the boundaries ∂R and $\partial\Omega$. Note that the MAD is measured in μm (1 pixel = $50\mu m$).

These measures, D, S, P and MAD, involve an available reference volume R. Recall that in the experiments we propose, this reference volume is given by interpolation of contours manually drawn in 2D sections by a dermatologist.
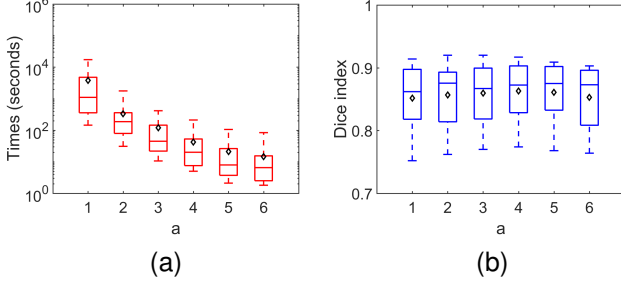
Fig. 1. Evaluation of the solver. LLCH-Exact segmentation of the 12 tumors of the clinical dataset for different grid sizes: $a = \{1, 2, 3, 4, 5, 6\}$. Black diamonds are the averaged values. (a) Segmentation time. (b) Dice index $D(\Omega, R)$ of the segmented volume with respect to reference contour R.

Practically, we consider 50 values of intensity I between 0 and $max(I_{\mathbf{x}})$ and remove the gel area (black area above the epidermis, see Fig. 2c) before the tumor segmentation is performed. The segmentation process is stopped when the volume change between two steps is less than 0.001% of the segmented volume. This applies for all the tests and for all the methods described in the following.

We evaluate the accuracy of the segmentation on a grid as a function of the grid size a, with $a = \{1, 2, 3, 4, 5, 6\}$ in pixels. The 12 images of the clinical dataset used are of size $300 \times 299 \times 832$, with about 75 millions voxels, and the largest region of interest is of size $232 \times 180 \times 226$, with about 9 millions voxels. The initialization volume is inside the tumor. The parameters are chosen as follows: for a fixed scale a, $\alpha \in [0.02, 2.4]$, $\delta t \in [0.1, 1]$, $\epsilon \in [1/\mathcal{N}, 4/\mathcal{N}]$ ($\mathcal{N} = \max(N_x, N_y, N_z)$ where N_x, N_y, N_z correspond respectively to the dimension of the image in each direction x, y and z). These parameters are adaptively tuned to maximize the Dice index. Fig. 1 shows the evolutions of the average computational time and of the average Dice index with respect to the grid size. The average time decreases rapidly as a increases and becomes acceptable for $a = 4$. It yields a speedup factor of 90 compared to the fine grid with $a = 1$. The average Dice index remains almost unchanged. It varies between 0.852 and 0.863. This means that the grid size does not affect significantly the result of the segmentation.

One important feature of the proposed algorithm is that it produces a diffuse interface or transition layer with thickness of order ϵ. This transition layer can be though as a fuzzification of the sharp contour to be detected. We illustrate now the key role that the parameter ϵ plays in improving sensitivity. We set $\alpha = 0.2$, $\delta t = 0.1$ and make ϵ vary from 0.009 to 0.038. As shown in Fig. 2, both the Dice index and the sensitivity increase when ϵ increases. Note also that if ϵ is too small, the active contour does not move because the transition layer does not exist yet. If ϵ is too large, the segmentation fails to be accurate.

IV. VALIDATION AND COMPARISONS WITH REFERENCE METHODS ON A CLINICAL DATASET

In this section we compare the results obtained following the proposed approach with those given by two reference

methods, namely the Mumford-shah Cahn-Hilliard (MSCH [9]) and the adaptative Log-Likelihood Level-Set (AdLL [4]) methods. These latters are based on variational formulations. Tab. 1 shows the terms involved in (1) for the two methods (see [9] and [4] for details). LLCH-exact and MSCH methods share the same regularization term. The data attachment term of the MSCH method is the piecewise constant Mumford-Shah functional. We refer to [4] for the validation of the AdLL method.

For the purpose of a fair comparison between LLCH-exact and MSCH methods, we propose, beside the implementation by Algorithm 1, another implementation using a Backward Euler scheme for the computation of the data attachment term. Practicaly, it consists in replacing the equation (23) by: $U^n \leftarrow (U^n - \delta t T_B)/(1 - \delta t T_A)$. In the sequel, we refer to this alternative implementation as LLCH-BE method. Since the choice of the regularization parameter α depends on the method used, we write $\alpha = \alpha_{LLCH-exact}$ (resp. $\alpha = \alpha_{LLCH-BE}$, α_{MSCH}, α_{AdLL}) when dealing with the LLCH-exact (resp. LLCH-BE, MSCH, AdLL) method.

A. Validation using synthetic tumor images

Two phantom volumes are generated with different scatterer densities in the dermis, epidermis and tumor, see Fig. 3. The various parameters are chosen as follows. The regularization parameter ranges are: $\alpha_{LLCH-exact} \in [0.03, 0.7]$, $\alpha_{LLCH-BE} \in [0.025, 0.3]$, $\alpha_{AdLL} \in [0.04, 2]$ and $\alpha_{MSCH} = \gamma/\max(N)^2$ where $\gamma \in [0.6, 10]$. The diffuse interface thickness range is: $\epsilon \in \{1/\mathcal{N}, 2/\mathcal{N}\}$ (LLCH-exact, LLCH-BE and MSCH methods). The time step δt must be chosen not too large when applying LLCH-exact and LLCH-BE methods: $\delta t \in [0.1, 1]$. On the contrary, it must be chosen large when applying MSCH and AdLL methods: $\delta t \in [40, 50]$ and $\delta t \in [0.5, 10]$, respectively. The AdLL method involves an additional parameter (threshold) T (see [4]). In what follows $T \in [2, 20]$. All these parameters are tuned adaptively in order to maximize the Dice index. The grid size is fixed, with $a = 4$, for all methods.

The two synthetic tumors are quite different: one is connected and the other has two connected components. A major asset of the proposed approach, is that it is robust to initialization changes, from volume inside the tumor to volume covering the tumor. We discuss now this point in more detail. As shown by Fig. 3 and Tab. II, the four studied methods give satisfactory resuts in cases (a) and (b), that is for initialization inside the tumor. LLCH-exact and LLCH-BE methods perform slightly better. It is dramatically different in cases (c) and (d), that is for initialization covering the tumor. MSCH segmentation fails in both cases (c) and (d) and gives unusable results. AdLL segmentation does not detect one of the component in case (c) and gives a quite poor Dice index in case (d). This illustrates one of the defects of this last method mentioned in the introduction: level set segmentations tend to underestimate the size of tumors. It is worth noting that the results remain unchanged for both the LLCH-exact and LLCH-BE segmentations.

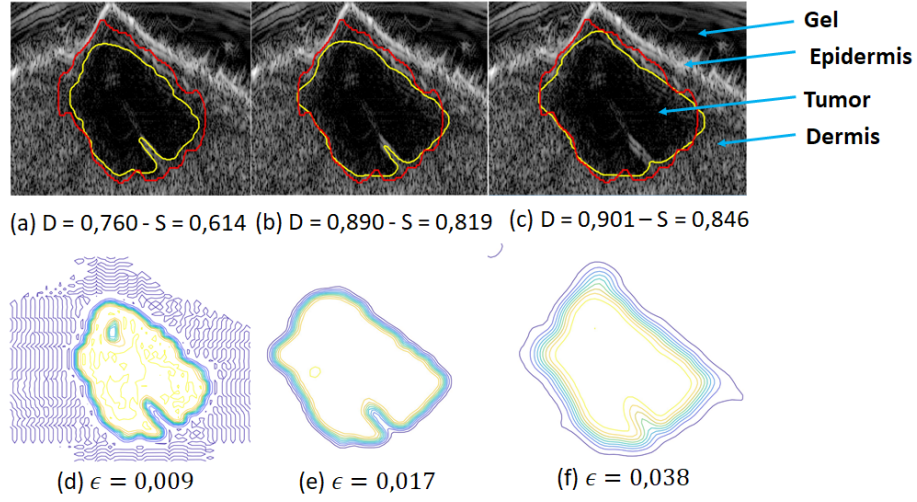These first experiments show clearly that the propose approach has some major advantages over the reference ones.

Fig. 2. Influence of the thickness of the diffuse interface illustrated on slices of tumor 8 LLCH-Exact segmention (Fig. 4h). (a,b,c) Dice index and Sensitivity for three increasing values of ϵ, (d,e,f). The more the transition layer expands, the better the Dice index and the sensitivity S become. The yellow contour is the slice of the segmented volume and the red contour is the reference contour drawn nanually by a dermatologist.

TABLE I
DATA ATTACHMENT AND REGULARIZATION TERMS OF THE TWO REFERENCE METHODS: MSCH [9] AND ADLL [4]

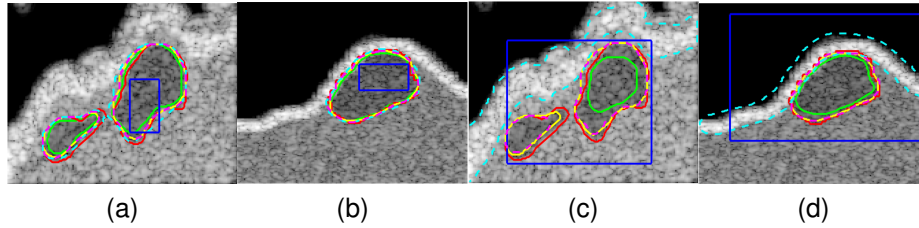| Term / Method	Data attachment	Regularization
MSCH	$\frac{1}{2}\left[\int u^2(I-c_1)^2 d\mathbf{x} + \int (u-1)^2(I-c_2)^2 d\mathbf{x}\right]$	$E_\epsilon^{CH}(u)/c_W$
AdLL	$|\nabla\phi|\log(\widehat{P}_A(I_\mathbf{x})/\widehat{P}_B(I_\mathbf{x}))$	$|\nabla\phi|\nabla.(\phi/|\nabla\phi|)$

Fig. 3. Validation using synthetic tumor images. Slice of the segmentation result. LLCH-exact: yellow solid line, LLCH-BE: pink dash line, MSCH: cyan dash line and AdLL: green solid line. The blue box is the slice of the initialization volume, inside the tumor, (a), (b), and covering the entire tumor, (c), (d). The red contour is the reference contour drawn manually by a dermatologist.

TABLE II
DICE INDEX OF THE SEGMENTATION OF SYNTHETIC IMAGES (FIG. 3)
WITH THE FOUR METHODS: LLCH-EXACT (ALGORITHM 1), LLCH-BE,
ADLL [4] AND MSCH [9].

Fig. 3 / Method	(a)	(b)	(c)	(d)
LLCH-exact/BE	**0.872**/ **0.876**	0.934/**0.942**	**0.872**/ 0.864	0.922/**0.932**
AdLL	0.826	0.898	0.405	0.773
MSCH	0.847	0.933	3×10^{-5}	0.027

These advantages may be greatly useful for medical applications.

B. Comparisons on a clinical dataset

Now, we propose experiments using the 12 tumor images of the clinical dataset. As before, we discuss the influence of the initialization. The parameters are chosen as follows.

- LLCH-exact: $\alpha_{LLCH-exact} \in [0.09, 1]$, $\delta t \in [0.1, 1]$ and $\epsilon \in [1/\mathcal{N}, 5/\mathcal{N}]$.
- LLCH-BE: $\alpha_{LLCH-BE} \in [0.05, 2.5]$, $\delta t \in [0.1, 1]$ and $\epsilon \in [1/\mathcal{N}, 5/\mathcal{N}]$.
- AdLL: $\alpha_{AdLL} \in [0.03, 0.8]$, $\delta t \in [2, 10]$ and $T \in [2, 10]$.
- MSCH: $\alpha_{MSCH} \in [\gamma/\max(N)^2]$ with $\gamma \in [1.5, 100]$, $\delta t \in [10, 20]$ and $\epsilon \in [1/\mathcal{N}, 10/\mathcal{N}]$.

All these parameters are tuned adaptively in order to maximize the Dice index for each tumor. The grid size is fixed, with $a = 4$, for all methods. All computations are performed under Matlab by a single machine with the core i7 processor 6500U, 2.5 GHz and 16GB of RAM.

1) Initialization inside the tumor: Results of the segmentation are shown in Fig. 4. Tab. III summarizes all the results for the Dice index, MAD, sensitivity S and precision P. The sensitivity S is high if the segmented volume covers a large part of the tumor and the precision P is high if the segmented volume is really part of the tumor. As in the
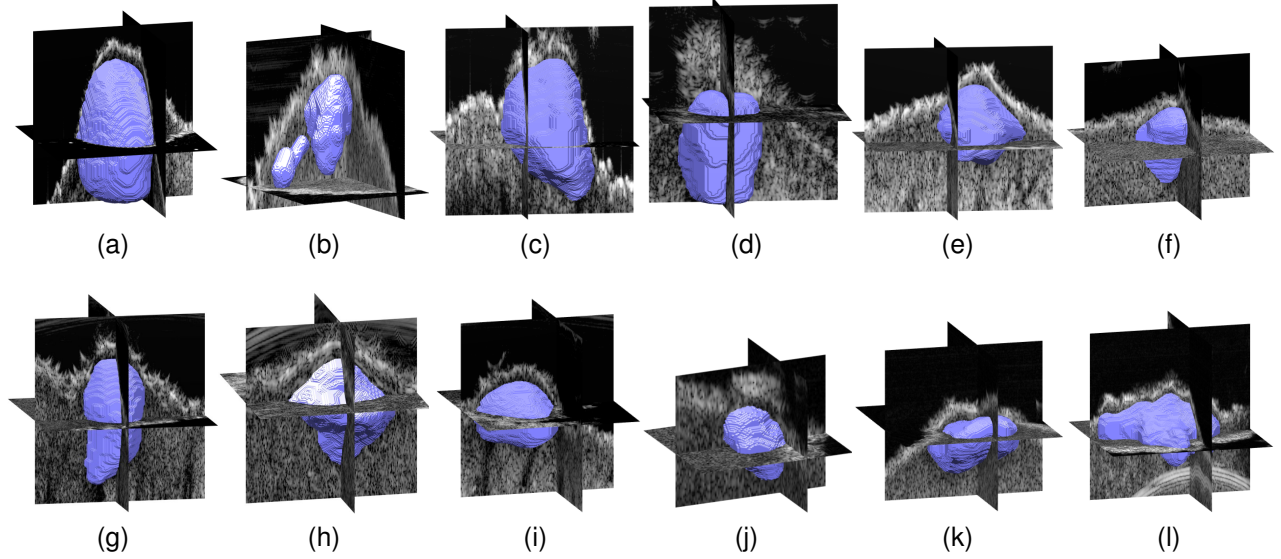
Fig. 4. Results of the LLCH-exact segmentation for the 12 tumors of the clinical dataset. (a) Tumor 1. (b) Tumor 2. (c) Tumor 3. (d) Tumor 4. (e) Tumor 5. (f) Tumor 6. (g) Tumor 7. (h) Tumor 8. (i) Tumor 9. (j) Tumor 10. (k) Tumor 11. (l) Tumor 12.

case of the two synthetic tumor images, the four studied methods give satisfactory results in terms of Dice index, the LLCH-exact and LLCH-BE methods performing slightly better. However, we may notice that the Dice index for the MSCH method is a bit lower than the others. This method is not really appropriate to segment clinical images which have very low contrast and complex shapes. In particular, a closer look at the segmentation of tumor 2 shows that the MSCH segmentation fails to detect the smallest component of the tumor. It can be also seen that it fails to detect the entire tumor 10, the segmented region corresponding to the epidermis. As expected, the sensitivity of the AdLL is low compared to the sensitivity of the LLCH-exact method with a significant difference of 12%. Since AdLL and LLCH-exact methods share the same data attachment term, this difference is due only to the choice of the regularization term, and more precisely to the flexibility introduced by the transition layer. With no suprise, the AdLL method gives the best precision. But it is worth noting that the LLCH-exact method has also a good precision. Concerning the MAD measure, the difference between LLCH-exact and AdLL methods is also significant. It is about 21%. It appears that the MSCH method is the worst method for this criterium. The AdLL method has the best precision, but significantly lower sensitivity and MAD. These results show on one hand, that the segmented volumes obtained by level set methods are small and far from the true boundary, and on the other hand, that our approach is relevant to tackle the problem of underestimation.

Compared to the intra-observability, our approach gives similar Dice index, sensitivity and precision with a faster execution time. However, the LLCH-exact method gives a slightly higher MAD. This means that our algorithm is still less accurate than the manual expert segmentation. The trade-off diagrams of Fig. 5 allow to visualize more precisely the main differences between the four methods. For an accurate

TABLE III
AVERAGED ACCURACY OF THE SEGMENTATION: PROPOSED LLCH-EXACT METHOD (ALGORITHM 1), LLCH-BE METHOD (ALTERNATIVE IMPLEMENTATION), AdLL METHOD [4] AND MSCH METHOD [9]. THE INDICATED VALUES ARE MEAN AND STANDARD DEVIATION ($\pm$) OVER ALL CASES WITH THE VOLUME INITIALIZATION INSIDE THE TUMOR.

Method / Index	LLCH-exact	LLCH-BE	AdLL	MSCH	Intra-ob
Dice	**0.862** $\pm$ 0.053	0.861 $\pm$ 0.049	0.826 $\pm$ 0.061	0.769 $\pm$ 0.247	0.864 $\pm$ 0.051
S	**0.853** $\pm$ 0.049	0.838 $\pm$ 0.073	0.763 $\pm$ 0.081	0.778 $\pm$ 0.248	0.855 $\pm$ 0.070
P	0.874 $\pm$ 0.073	0.891 $\pm$ 0.069	**0.910** $\pm$ 0.086	0.776 $\pm$ 0.258	0.879 $\pm$ 0.068
MAD (μm)	**191** $\pm$ **68**	194 $\pm$ 72	231 $\pm$ 79	320 $\pm$ 222	177 $\pm$ 60
Times (s)	41.0	57.0	14.7	**13.4**	300

segmentation, both the sensitivity and the precision should be as close to 1 as possible. Recall that the Dice index D is given by $D = 2/(1/S + 1/P)$. The level curves of the Dice index are drawn in gray. We propose also in Fig. 6, examples of segmentation that illustrate the difference of behavior between LLCH-exact and AdLL methods.

2) Initialization covering the tumor: Now, we propose experiments to test the robustness to intialization changes, from volume inside the tumor to volume covering the tumor. The aim is to confirm the results already described in the case of synthetic tumor images. As shown in the table IV. LLCH-exact and LLCH-BE methods have Dice index and MAD measure quite similar to those obtained for initialization inside the tumor, with a difference less than 5%. As before, the LLCH-exact method yields the best results. The AdLL and MSCH segmentations fail in almost all cases and give very poor averaged Dice index and MAD measure. As shown in Fig. 7, in the case of tumor 6, the segmented volume for the AdLL segmentation is unusable whereas the result is still very good for the LLCH-exact segmentation.

V. DISCUSSION

One of the main topics of this work is to emphasize the advantages of the regularization term $E_\epsilon^{CH}(u)/c_W$ over the

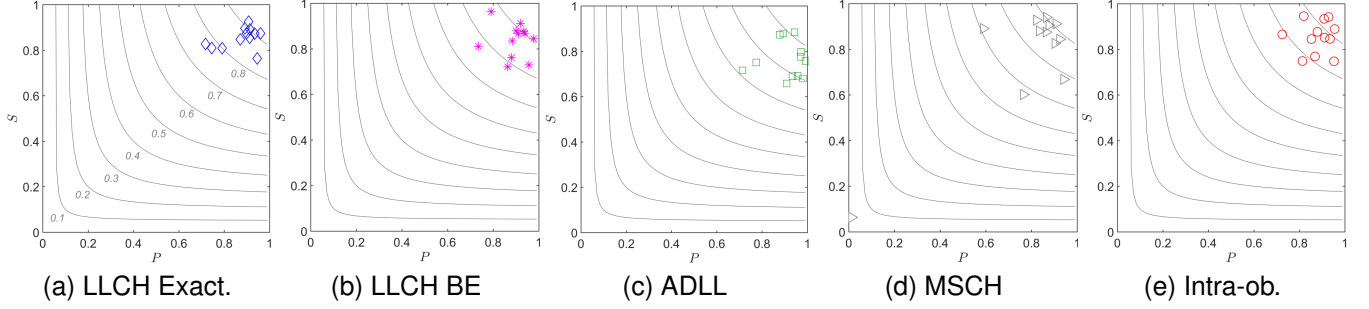(a) LLCH Exact. (b) LLCH BE (c) ADLL (d) MSCH (e) Intra-ob.

Fig. 5. Sensitivity S versus precision P for the studied segmentation methods. For an accurate segmentation, both the sensitivity and the precision should be as close to 1 as possible. The Dice index D is given by $D = 2/(1/S + 1/P)$. The level curves of the Dice index are drawn in gray. (a) LLCH-exact method with the best sensitivity/precision trade-off. (b) LLCH-BE method with results comparable to LLCH-exact method. (c) ADLL method with low sensitivity. (d) MSCH method: in some cases the sensitivity and/or precision is too low. (e) Intra-observer variability.
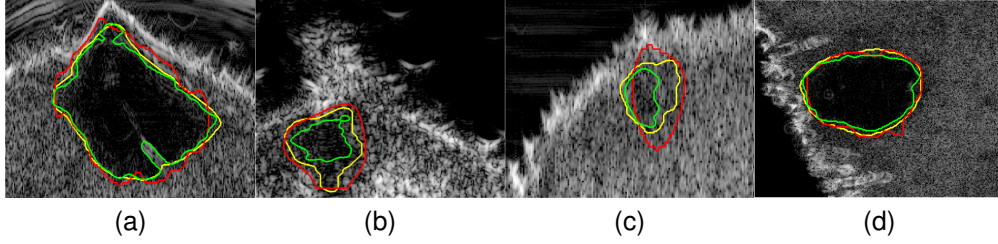

(a) (b) (c) (d)

Fig. 6. Comparisons between LLCH-exact and AdLL methods. Slices of 4 segmentations: LLCH-exact contours in yellow, AdLL contours in green, reference contours in red.

widely used level set term $|\nabla\phi|\nabla.(\phi/|\nabla\phi|)$. However, as observed in section V, the MSCH method gives quite poor results. In fact, the data attachment term in this case, *i.e.* the piecewise constant Mumford-Shah functional, is not adapted to ultrasound images. The regularization term $E_\epsilon^{CH}(u)/c_W$ is unable to correct this problem. The log-likelihood distance between intensity distributions inside and outside the tumor, $LL(u)$, seems to be a relevant data attachment term, especially when using nonparametric estimations. Combined with this data attachment term, the regularization term $E_\epsilon^{CH}(u)/c_W$ performs much better than the level set term $|\nabla\phi|\nabla.(\phi/|\nabla\phi|)$. On one hand, for initialization inside the tumor, the LLCH-exact method yields the best Dice index, MAD measure and sensitivity with a good precision. This means that the LLCH-exact method is well-designed to tackle the problem of underestimation of tumor volumes. On the other hand, it is the only method (with the alternative implementation LLCH-BE) that is robust to initialization changes from volume inside the tumor to volume covering the tumor, the parameters remaining

unchanged.

As discussed before, the multi-grid implementation does not affect significantly the result of the segmentation. Working on a grid with $a = 4$ yields a speed-up factor of 90. The computational time of the LLCH-exact method is twice the computational time of the AdLL method when the initialization volume is inside the tumor. It is slightly smaller when the initialization volume covers the tumor. A parallel C++ implementation of the proposed LLCH-exact algorithm using Open MP allows to divide the computational time by a factor 4.

We end this discussion by giving some precisions about the choice of the three parameters δt (time step), ϵ (size of the diffuse interface) and α (smoothness of the moving interface). Concerning the time step, MSCH and AdLL methods require large δt to ensure that the contour can move. On the contrary, LLCH-exact and LLCH-BE mehods give the best results for $\delta t \in [0.1, 1]$, whereas too large time steps can give inaccurate segmentations. The width ϵ is chosen with respect to the order
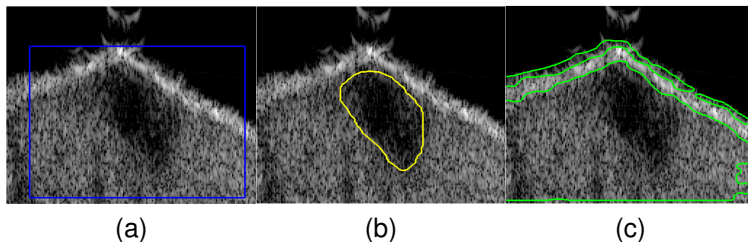

(a) (b) (c)

Fig. 7. Initialization covering the tumor. (a) Slice of the initial volume for tumor 6, see Fig. 4f. (b) Slice of the segmented volume using the LLCH-exact method. (c) Slice of the segmented volume using the AdLL method.

Method Index	LLCH-exact	LLCH-BE	AdLL	MSCH
Dice	**0.860** ± 0.052	0.849 ± 0.065	0.540 ± 0.266	0.594 ± 0.316
MAD (μm)	**196** ± 73	207 ± 74	854.8 ± 499.1	762.2 ± 682.1
Times (s)	57.8	72.4	78.1	**23.4**

of the mesh grid size. If ϵ is too small, the transition layer does not move and numerical problems such as stiff problems can appear. In the experiments we propose, these three parameters are adaptively tuned in order to maximize the Dice index. This is justified by the fact that the Dice index takes into account both the sensitivity and the precision.

VI. CONCLUSION

We have proposed a new method for skin tumor segmentation in 3D ultrasound images. Our motivation was to overcome the fact that level set segmentations tend to underestimate segmented volumes and are not robust to initialization changes. We have introduced a reaction diffusion PDE as a regularization term of a variational formulation, with a data attachment term given by a log-likelihood distance between intensity distributions. This PDE, the Allen-Cahn equation, aims at describing diffuse interface phase field evolutions. We have shown that, thanks to the flexibility introduced by the diffuse interface and thanks to an exact implementation, the new approach, *i.e.* the LLCH-exact method, has some major advantages over reference ones. Especially, experiments on synthetic and clinical data have shown that the LLCH-exact segmentation is well-designed to tackle the problem of underestimation of tumor volumes, and is robust to initialization changes, from volume inside the tumor to volume covering the tumor. The multi-grid implementation that we have proposed allows to obtain reasonable computational times for medical applications.

APPENDIX
GRADIENT DESCENT OF THE ENERGY E_ϵ

We only need to compute the functional derivative $\delta S_A/\delta u$ with S_A given by formula (13). We have

$$\frac{\delta S_A}{\delta u} = \frac{\delta |\Omega_A|}{\delta u} \sum_I \hat{P}_A(I) \log \hat{P}_A(I)$$
$$+|\Omega_A| \sum_I \frac{\delta \hat{P}_A(I)}{\delta u} \log \hat{P}_A(I) + |\Omega_A| \sum_I \frac{\delta \hat{P}_A(I)}{\delta u} \tag{38}$$

Since $|\Omega_A| = \int_{\Omega_A} d\mathbf{x} \simeq \int_\Omega u^2 d\mathbf{x}$, assuming $K_\lambda(I(\mathbf{x}) - I) \simeq \delta(I(\mathbf{x}) - I)$, where δ is the Dirac distribution, we have

$$|\Omega_A|\hat{P}_A(I) = \int u^2 \delta(I(\mathbf{x}) - I) d\mathbf{x} \tag{39}$$

$$\frac{\delta |\Omega_A|}{\delta u} \hat{P}_A(I) + |\Omega_A| \frac{\delta \hat{P}_A(I)}{\delta u} = 2u\delta(I(\mathbf{x}) - I) \tag{40}$$

$$|\Omega_A| \frac{\delta \hat{P}_A(I)}{\delta u} = 2u[\delta(I(\mathbf{x}) - I) - \hat{P}_A(I)] \tag{41}$$

Consequently, we obtain

$$\frac{\delta S_A}{\delta u} = 2u \sum_I \hat{P}_A(I) \log \hat{P}_A(I)$$
$$+ \sum_I 2u[\delta(I(\mathbf{x}) - I) - \hat{P}_A(I)] \log \hat{P}_A(I) \tag{42}$$
$$+ \sum_I 2u[\delta(I(\mathbf{x}) - I) - \hat{P}_A(I)]$$

and

$$\frac{\delta S_A}{\delta u} = 2u \sum_I \delta(I(\mathbf{x}) - I) \log \hat{P}_A(I)$$
$$+2u \sum_I \delta(I(\mathbf{x}) - I) - 2u \sum_I \hat{P}_A(I) \tag{43}$$

We have also

$$\sum_I \delta(I(\mathbf{x}) - I) \log \hat{P}_A(I) \simeq \delta * \log \hat{P}_A(I(\mathbf{x}))$$
$$= \log \hat{P}_A(I(\mathbf{x})) \tag{44}$$

$$\sum_I \delta(I(\mathbf{x}) - I) \simeq \delta * 1 = 1 \tag{45}$$

$$\sum_I \hat{P}_A(I) = 1 \tag{46}$$

This means that

$$\frac{\delta S_A}{\delta u} = -2u \log \hat{P}_A(I(\mathbf{x})) \tag{47}$$

We obtain in the same way

$$\frac{\delta S_B}{\delta u} = -2(u - 1) \log \hat{P}_B(I(\mathbf{x})) \tag{48}$$

ACKNOWLEDGMENT

REFERENCES

[1] X. Yuan, N. Situ, G. Zouridakis, *A narrow band graph partitioning method for skin lesion segmentation*, Pattern Recognition, vol. 42, pp. 1017-1028, 2009.

[2] M. Mete, N. M. Sirakov, *Dermoscopic diagnosis of melanoma in a 4D space constructed by active contour extracted features*: Computerized Medical Imaging and Graphics, vol. 36, pp. 572-579, 2012.

[3] M. Pereyra, N. Dobigeon, H. Batatia, J. Tourneret, *Segmentation of skin lesions in 2D and 3D ultrasound images using a spatially coherent generalized rayleigh mixture model*, Medical Imaging, IEEE Transactions on, pp. 1509-1520, 2012.

[4] B. Sciolla, L. Cowell, T. Dambry, B. Guibert and P. Delachartre, *Segmentation of Skin Tumors in High-Frequency 3-D Ultrasound Images*, Ultrasound in Medicine & Biology, vol. 45, no. 1, pp. 227-238, 2017.

[5] Y. Sun, C. Beckermann, *Sharp interface tracking using the phase field equation*: Journal of Computational Physics, vol. 220, pp. 626-653, 2007.

[6] S. M. Allen and J. W. Cahn, *A microscopic theory for anti-phase boundary motion ad its application to anti-phase domain coarsening*, Acta Metall, vol. 27, pp. 1085-1095, 1979.

[7] C. M. Elliott, *The Cahn-Hilliard model for the kinetics of phase separation*, International Series of Numerical Mathematics vol. 88, pp. 36-73, 1989.

[8] E. G. Morton, *Generalized Ginzburg-Landau and Cahn-Hilliard equations based on a microforce balance*, Physica D: Nonlinear Phenomena vol. 92, pp. 3-4, 1999.

[9] S. Esedoglu and Y. H. R. Tsai, *Threshold dynamics for the piecewise constant Mumford-Shah functional*, Journal of Computational Physics vol. 211, pp. 367-384, 2006.

[10] Y. Li and J. Kim, *Multiphase image segmentation using a phase-field model*, Computers and Mathematics with Applications vol. 62, pp. 737-745, 2011.

[11] S. Zhao, M. Zhou, T. Jia, P. Xu, Z. Wu, Y. Tian, Y. Peng and J. S. Jin, *Multi-branched cerebrovascular segmentation based on phase field and likelihood model*, Computers & Graphics vol. 38, pp. 239-247, 2014.

[12] M. H. R. Cardinal, J. Meunier, G. Soulez, R. L. Maurice, E. Therasse and G. Cloutier, *Intravascular Ultrasound Image Segmentation: A Three-Dimensional Fast-Marching Method Based on Gray Level Distributions*, IEEE Transactions on Medical Imaging, vol. 25, no. 5, pp. 590-601, 2006.

[13] G. Slabaugh, G. Unal, M. Wels, T. Fang and B. Rao, *Statistical Region-Based Segmentation of Ultrasound Images*, Ultrasound in Medicine & Biology, vol. 35, no. 5, pp. 781-795, 2009.

[14] B. Sciolla, J. L. Digabel, G. Josse, T. Dambry, P. Delachartre, *Joint segmentation and characterization of the dermis in 50 Mhz ultrasound 2D and 3D images of the skin*, Computers in Biology and Medicine , vol. 00, pp. 1-17, 2018.

[15] E. Parzen, *On Estimation of a Probability Density Function and Mode*, Annals of Math. statistics, vol. 33, Issue 3, pp. 1065-1076, Sep. 1962.

[16] J. Kim, J. Fisher, A. Yezzi, M. Cetin, A. Willsky, *A non parametric statistical method for image segmentation using information theory and curve evolution*, Image processing. IEEE, vol. 14, pp. 1486-1502, 2005.

[17] B. Sciolla, P. Ceccato, L. Conwell, T. Dambry, B. Guibert and P. Delachartre, *Segmentation of inhomogeneous skin tissues in high-frequency 3D ultrasound images, the advantage of non-parametric log-likelihood methods*, Physics Procedia, 70 (2015), pp. 1177-1180.

[18] F. Destrempes and G. Cloutier, *A critical review and uniformized representation of statistical distributions modeling the ultrasound echo envelope*, Ultrasound in Medicine and Biology, 2010, 36, pp. 1037-1051.

[19] S. Osher and J. A. Sethian, *Fronts propagating with curvature dependent speed : Algorithm based on hamilton jacobi formulations*, Journal of Computational Physics, vol. 79, issue 1, pp. 12-49, 1988.

[20] A. Braides, $\Gamma-$convergence for beginners, Oxford University Press, 2002.

[21] L. Modica and S. Mortola, *Un esempio di gamma-convergenza*, Boll. Un. Math. Ital. vol. 14, no. 1, pp. 285-299, 1977.

[22] T. M. Cover and Y. A. Thomas, *Elements of Information Theory*, John Wiley and Sons, Inc., 1991.

[23] W. Hundsdorfer, J. G. Verwer, *Numerical Solution of Time-Dependent Advection-Diffusion-Reaction Equations*, Springer-Verlag, Berlin, 2003.